their fits use a prefactor T_θ^0 whose weak T-dependence disagrees with our continuum two-dimensional theory. We speculate that this can be explained by corrections to scaling: there is an appreciable density of fermionic carriers not bound into Cooper pairs, and this would reduce the effective bosonic superfluid density which enters our scaling forms with a T-dependent factor. Corson *et al.*[4] motivated the scaling using the vortex theory[18], but did not consider bound vortex pairs, whose contributions do not obey their scaling assumptions.

We have delineated the distinct dynamic regimes of thermally fluctuating superconductors: the low-T phase-only hydrodynamics, the classical vortex hydrodynamics in the vicinity of T_{KT}, and the quantum-critical region where phase and vortex fluctuations strongly coupled—here we proposed a dynamical model in which non-linear 'mode-coupling' terms demanded by the Poisson bracket, equation (6), dominate the universal, low-frequency, dissipative dynamics. Our approach could be extended to other two-dimensional systems, such as the magnetic-field-tuned superconductor–insulator transition, where a coupling to the external field would be required in equation (4), and quantum Hall transitions.□

Received 12 January; accepted 4 April 2000.

1. Rimberg, A. J. *et al.* Dissipation-driven superconductor-insulator transition in a two-dimensional Josephson-junction array. *Phys. Rev. Lett.* **78,** 2632–2635 (1997).
2. Chervenak, J. A. & Valles, J. M. Observation of critical amplitude fluctuations near the two-dimensional superconductor-insulator transition. *Phys. Rev. B* **59,** 11209–11212 (1999).
3. Marković, N., Christiansen, C., Mack, A. M., Huber, W. H. & Goldman, A. M. Superconductor-insulator transition in two dimensions. *Phys. Rev. B* **60,** 4320–4328 (1999).
4. Corson, J., Mallozzi, R., Orenstein, J., Eckstein, J. N. & Bozovic, I. Vanishing of phase coherence in underdoped $Bi_2Sr_2CaCu_2O_{8+\delta}$. *Nature* **398**, 221–223 (1999).
5. Uemura, Y. J. *et al.* Universal correlations between T_c and n_s/m (carrier density over effective mass) in high-T_c cuprate superconductors. *Phys. Rev. Lett.* **62**, 2317–2320 (1989).
6. Doniach, S. & Inui, M. Long-range Coulomb interactions and the onset of superconductivity in the high-T_c materials. *Phys. Rev. B* **41**, 6668–6678 (1990).
7. Fisher, M. P. A., Grinstein, G. & Girvin, S. M. Presence of quantum diffusion in two dimensions: Universal resistance at the superconductor-insulator transition. *Phys. Rev. Lett.* **64,** 587–590 (1990).
8. Trivedi, N. & Randeria, M. Deviations from Fermi-liquid behavior above T_c in 2D short coherence length superconductors. *Phys. Rev. Lett.* **75,** 312–315 (1995).
9. Emery, V. J. & Kivelson, S. A. Importance of phase fluctuations in superconductors with small superfluid density. *Nature* **374,** 434–437 (1995).
10. Emery, V. J. & Kivelson, S. A. Crossover and phase coherence in cuprate superconductors. *J. Phys. Chem. Solids* **59,** 1705–1710 (1998).
11. Sondhi, S. L., Girvin, S. M., Carini, J. P. & Shahar, D. Continuous quantum phase transitions. *Rev. Mod. Phys.* **69,** 315–333 (1997).
12. Sachdev, S. *Quantum Phase Transitions* (Cambridge Univ. Press, Cambridge, 1999).
13. Doniach, S. Quantum fluctuations in two dimensional superconductors. *Phys. Rev. B* **24,** 5063–5070 (1981).
14. Sachdev, S. Theory of finite-temperature crossovers near quantum critical points close to, or above, their upper-critical dimension. *Phys. Rev. B* **55,** 142–163 (1997).
15. Sachdev, S. Universal relaxational dynamics near two-dimensional quantum critical points. *Phys. Rev. B* **59,** 14054–14073 (1999).
16. Khalatnikov, I. M. *An Introduction to the Theory of Superfluidity* (W. A. Benjamin, New York, 1965).
17. Popov, V. N. *Functional Integrals in Quantum Field Theory and Statistical Physics* (D. Reidel, Boston, 1983).
18. Ambegaokar, V., Halperin, B. I., Nelson, D. R. & Siggia, E. D. Dissipation in two dimensional superfluids. *Phys. Rev. Lett.* **40,** 783–786 (1978).
19. Damle, K. & Sachdev, S. Nonzero-temperature transport near quantum critical points. *Phys. Rev. B* **56,** 8714–8733 (1997).
20. Herbut, I. F. Finite temperature transport at the superconductor-insulator transition in disordered systems. *Phys. Rev. Lett.* **81,** 3916–3919 (1998).
21. Chubukov, A. V., Sachdev, S. & Ye, J. Theory of two-dimensional quantum Heisenberg antiferromagnets with a nearly critical ground state. *Phys. Rev. B* **49,** 11919–11961 (1994).
22. Fisher, M. P. A. Quantum phase transitions in disordered two-dimensional superconductors. *Phys. Rev. Lett.* **65,** 923–926 (1990).
23. Sudbø, A., Nguyen, A. K. & Hove, J. Anomalous scaling dimensions and critical points in type-II superconductors. Pre-print cond.mat/9907386 at ⟨xxx.lanl.gov⟩ (1999).
24. Sachdev, S. & Ye, J. Universal quantum-critical dynamics of two-dimensional antiferromagnets. *Phys. Rev. Lett.* **69,** 2411–2414 (1992).
25. Wagenblast, K.-H., van Otterlo, A., Schön, G. & Zimányi, G. T. Superconductor-insulator transition in a tunable dissipative environment. *Phys. Rev. Lett.* **79,** 2730–2733 (1997).
26. Dalidovich, D. & Phillips, P. Fluctuation conductivity in insulator-superconductor transitions with dissipation. *Phys. Rev. Lett.* **84,** 737–740 (2000).
27. Kawasaki, K. Kinetic equations and time correlation functions of critical fluctuations. *Ann. Phys. (N.Y.)* **61,** 1–56 (1970).
28. Hohenberg, P. C., Siggia, E. D. & Halperin, B. I. Density-correlation function of liquid helium near T_λ in the symmetric planar model. *Phys. Rev. B* **14,** 2865–2874 (1976).
29. Grempel, D. Comment on "Low-temperature behavior of two-dimensional quantum anti-ferromagnets". *Phys. Rev. Lett.* **61,** 1041 (1988).
30. Wagenblast, K.-H., van Otterlo, A., Schön, G. & Zimányi, G. T. New universality class at the superconductor-insulator transition. *Phys. Rev. Lett.* **78,** 1779–1782 (1997).

Acknowledgements

We thank J. Orenstein, D. Grempel and A. Sudbø for useful discussions, and the Division of Materials Theory of the National Science Foundation for support.

Correspondence should be addressed to S.S. (e-mail: subir.sachdev@yale-edu).

Optical microscopy using a single-molecule light source

J. Michaelis, C. Hettich, J. Mlynek & V. Sandoghdar

Fachbereich Physik and Optik-Zentrum Konstanz, Universität Konstanz, Fach M696, 78457 Konstanz, Germany

Rapid progress in science on nanoscopic scales has promoted increasing interest in techniques of ultrahigh-resolution optical microscopy. The diffraction limit can be surpassed by illuminating an object in the near field through a sub-wavelength aperture at the end of a sharp metallic probe[1,2]. Proposed modifications[3,4] of this technique involve replacing the physical aperture by a nanoscopic active light source. Advances in the spatial[5] and spectral[6] detection of individual fluorescent molecules, using near-field and far-field methods[7], suggest the possibility of using a single molecule[8,9] as the illumination source. Here we present optical images taken with a single molecule as a point-like source of illumination, by combining fluorescence excitation spectroscopy[10] with shear-force microscopy[11]. Our single-molecule probe has potential for achieving molecular resolution in optical microscopy; it should also facilitate controlled studies of nanometre-scale phenomena (such as resonant energy transfer) with improved lateral and axial spatial resolution.

Over nearly two decades the resolution in scanning near-field optical microscopy (SNOM) using aperture probes has levelled out at 3a value of ~50 nm. In addition to technological difficulties such as reproducibility of tip fabrication, the resolution in this mode of SNOM is fundamentally limited because the finite skin depth of real metals leads to a finite effective aperture size that one can achieve in the laboratory[3]. To overcome this problem, some researchers have pursued apertureless SNOM in which a sharp tip is used to scatter the near field of the sample[12], but in this configuration the resolution is limited by the radius of curvature of the probe used. The use of a nanoscopic active medium as a probe for SNOM has the advantage that its size can be reduced to that of a single atom or molecule. In this case, the resolution should only depend on the separation between the source and the sample.

Figure 1a shows the schematics of a combined scanning confocal microscope and scanning near-field optical microscope that constitutes the heart of our experimental setup[13] operating at $T = 1.4$ K. A commercial piezo-electric scanner controls the position of the sample in front of a tapered optical-fibre probe. A microscope objective with a numerical aperture of 0.8 can be used to illuminate the sample or to collect the light from it. For adjusting the focus of the objective and for positioning the fibre probe, home-made piezo-driven translation stages are used[14]. We use the shear-force signal from a quartz tuning fork to monitor or to regulate the separation between the sample surface and the probe[15]. In the experiments described here, the end of the fibre probe contained a micron-sized *p*-terphenyl crystal (see Fig. 1b) that was doped with terrylene molecules at a nominal concentration of about 10^{-7}. To prepare such a probe, we first co-sublimated *p*-terphenyl and terrylene to obtain crystals of the order of a few micrometres in size on a cover slide. The spatial doping concentration of the

microcrystals was then examined by collective excitation of the terrylene molecules at $\lambda = 514$ nm in a confocal arrangement under ambient conditions[16,17]. Once a microcrystal of a desired size and doping was located, it was carefully glued to the end of an uncoated chemically etched single-mode fibre, and this probe was transferred into the cryogenic setup indicated in Fig. 1a.

Individual terrylene molecules in the micro-crystal were identified by fluorescence excitation spectroscopy[10,18] at $T = 1.4$ K. The light of a ring-dye laser operating at $\lambda \approx 578$ nm was first intensity stabilized using an electro-optical modulator and then coupled into the optical fibre leading to the micro-crystal in the cryostat. Because the sharp zero-phonon lines of the terrylene molecules are inhomogeneously distributed in frequency space, individual molecules can become excited when scanning the laser frequency. The red-shifted fluorescence of a selectively excited molecule at $\lambda \approx 630$ nm is then detected by an avalanche photodiode after passing through the microscope objective and spectral filters. In this manner, we could typically record resonance lines narrower than 50 MHz, count rates of 100 kHz and a signal-to-noise ratio of the order of 100:1 (Fig. 1c). Aside from the exquisitely narrow spectral lines and a high signal-to-noise ratio, our system also proves to be extremely photostable in contrast to the dye molecules that are typically studied at room temperature[5]. These features are the main reason for choosing this system for our present work.

Once the laser was tuned into resonance with a single terrylene molecule, the probe was moved nearer the sample until the onset of a shear-force signal was observed at a separation of about 20 nm. The sample was then retracted to a given fixed axial position from the tip and scanned laterally while monitoring the shear-force signal as a safety measure. The sample consisted of 25 nm high triangular aluminium islands arranged in a hexagonal lattice with a period of 1.7 μm on a cover slide[19]. Figure 2a displays a topography image of the region that was studied in this experiment recorded with an atomic force microscope after the sample was taken out of the cryostat. The arrow indicates an area where a metallic island is largely missing, which results in two nanostructures. The image in Fig. 2b shows the raw fluorescence signal of a single molecule positioned in front of this sample just before the onset of the shear-force signal. The photon counts were integrated for 20 ms per pixel during which period the laser frequency was scanned back and forth once over an interval of ±250 MHz around the resonance to compensate for small laser drifts and occasional spectral diffusions[20]. As expected, the signal drops substantially each time a metallic island blocks the transmission of the molecular fluorescence. Although the triangular form of the islands does not manifest itself strongly, the image shows a striking reproducibility among different lattice periods. For example, the set of islands labelled *i* can clearly be distinguished from that labelled *ii* corresponding to the two possible orientations of the triangular structures. Also, the bright regions display a systematic pattern, with the exception of the area around the defect.

In Fig. 3 we show this image (Fig. 3e) together with three other optical images taken with the same single molecule at the same lateral position but with different distances between the crystal extremity and the sample (350 nm, 80 nm, 50 nm and 20 nm in Fig. 3a, b, d and e, respectively). The scans were recorded in the chronological order of Fig. 3b, a, e and d. These images are very lightly filtered by averaging the signal from each pixel with a weighting factor of 8 and its 8 neighbouring ones each with a weight of 1. To account for variations in the excitation intensity among different runs, the count rates in all four images have been normalized and a common colour scale is used so that one can compare them directly. Individual metallic islands and their hexagonal arrangement can be clearly identified in all cases, but the tiny defect structures give rise to a significant signal only at the smallest molecule–sample separation achieved in Fig. 3e. The fact that the contrast and the resolution are considerably worse at a larger distance also becomes evident when comparing Fig. 3a with the other images.

Bringing the sample closer in steps as small as 30 nm from Fig. 3b to d to e results in a substantial but continuous evolution of the bright and dark contrast patterns although these remain very robust within each figure. This can be seen more quantitatively in Fig. 3f where two cross-sections α and β exactly 1.7 μm apart are plotted. Note that the signal undergoes oscillations above and below the background indicated by a baseline. We attribute the origin of this effect and the rich images of individual metallic islands (for example, in Fig. 3e) to the polarization-sensitive interaction of the molecular dipole radiation with the aluminium triangles. Such interference-like phenomena have been reported in different

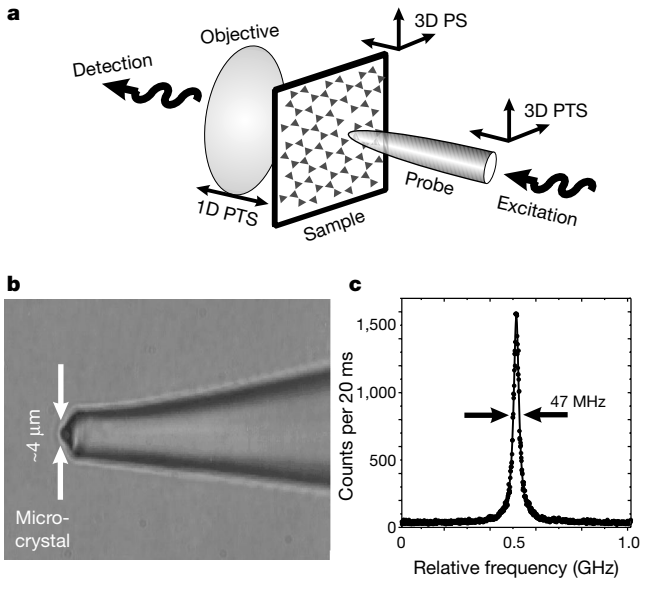

Figure 1 Overview of experimental features for realizing a single-molecule probe. **a**, Schematic view of the experimental configuration. PS, piezo-electric scanner; PTS, piezo-driven translation stage. See text for details. **b**, an optical microscope image of the fibre probe displaying a micro-crystal of *p*-terphenyl glued to its end. The micro-crystal was lightly doped with terrylene molecules. **c**, An excitation spectrum of the molecule used for recording the images in this experiment. The solid line shows a lorentzian fit to the data revealing a full-width at half-maximum of 47 MHz.

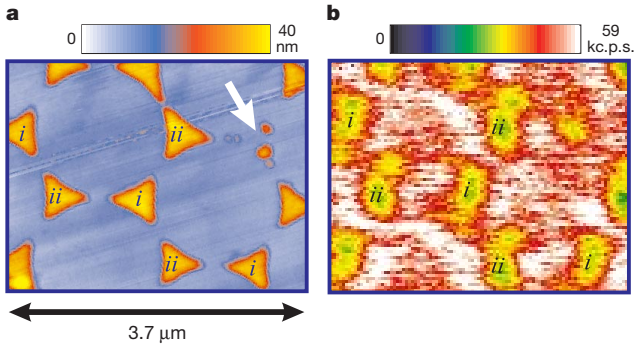

Figure 2 Topography and optical images of the sample. **a**, An atomic force microscope (AFM) topography image of the area of the sample used in this experiment. The arrow points to the remains of an island that is largely missing. We note that, although we have also recorded shear-force topography images of the sample taken at 1.4 K, because of our micrometre-size tip dimensions the resolution is not as good as that of an AFM. **b**, The optical raster-image recorded using the fluorescence of a single terrylene molecule for illumination. This scan contains 100 × 80 pixels with an integration time of 20 ms per pixel. The colour scale displays the raw experimental count rates in units of thousand counts per second (kc.p.s.).

experimental[21,22] and theoretical[23,24] works on conventional SNOM with polarized illumination. These studies have concluded that image interpretation becomes non-trivial for certain combinations of the electric field orientation and sample morphology and that the image quality depends on the illumination and detection polarization as well as the detection angle[22]. In the case of a single-molecule emitter, one should also take into account the modification of its spectral properties owing to the influence of the sample surface[25,26]. A detailed theoretical and experimental study of these properties will be the topic of a future publication.

Clearly, the complex contrast observed in the images complicates the assignment of a resolution. When dealing with finite-sized structures, one common method for evaluating the resolution is measuring the edge sharpness of the obtained signal[27]. In our case, however, following this guideline is not straightforward because of the oscillations about the background. We therefore merely note that the signal in Fig. 3f drops below the baseline from its 10% to 90% value over a length of about 180 nm which is less than one-third of the emission wavelength.

When extending the principles of scanning optical near-field microscopy to the case of a point-like electric dipole probe, the resolution is expected to depend only on the probe–sample separation. From a practical point of view, addressing molecules that lie very close to the probe end should lead to higher spatial resolution and in the extreme limit to a molecular resolution. To achieve this, we plan to use sub-micrometre crystals and implement various techniques for identifying single molecules at the end of the crystal, for example, through evanescent excitation. In addition to the detection of the fluorescence intensity, the internal quantum mechanical properties of the molecule such as fluorescence lifetime[26,28] and energy level shifts[26] can be used to extract information about its immediate environment. Our single-molecule probe could be also used to study a variety of phenomena such as surface-enhanced Raman spectroscopy and resonant energy transfer with an unprecedented lateral and axial spatial resolution. □

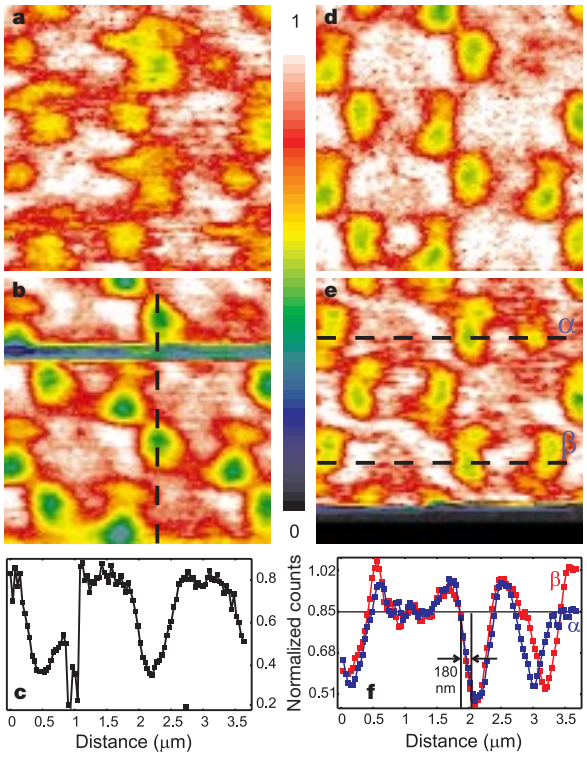

Figure 3 Images taken with the same molecule positioned at four different distances from the sample. These images are very lightly filtered (see text). The separation between the micro-crystal's extremity and the sample was 350 nm (**a**), 80 nm (**b**), 50 nm (**d**) and 20 nm (**e**). **e**, A more complete view of the run shown in Fig. 2b where in the last part the molecular spectrum became unstable and underwent a large jump of the order of hundred GHz (ref. 29) when the probe came into contact with the sample, so that a very small change in the shear-force signal was detected. **c**, The fluorescence signal along the cross-section shown in **b**. Note the sudden drop of the signal to ~200 counts per pixel (about 0.2 on the normalized scale) while our residual fluorescence corresponded to about 30 counts per pixel. Here the molecule has undergone a small spectral jump to the edge of the frequency scan range which was corrected for after a few scan lines by adjusting the laser frequency manually. **f**, the fluorescence signals along the two cross-sections α and β shown in **e**. A comparison of the four images taken over a period of over 2 h reveals the stability of the system and lack of any lateral drifts.

Received 20 January; accepted 15 March 2000.

1. Lewis, A., Isaacson, M., Muray, A. & Harootunian, A. Scanning optical microscopy with 500 Å spatial resolution. *Biophys. J.* **41,** 405 (abstr.) (1983).
2. Pohl, D. W., Denk, W. & Lanz, M. Optical stethoscopy: image recording with resolution λ/20. *Appl. Phys. Lett.* **44,** 651–653 (1984).
3. Liebermann, K., Harush, S., Lewis, A. & Kopelman, R. A light source smaller than the optical wavelength. *Science* **247,** 59–61 (1990).
4. Lewis, A. & Liebermann, K. Near-field optical imaging with a non-evanescently excited high-brightness light source of sub-wavelength dimensions. *Nature* **354,** 214–216 (1991).
5. Betzig, E. & Chichester, R. J. Single molecules observed by near-field scanning optical microscopy. *Science* **262,** 1422–1425 (1993).
6. Moerner, W. E. & Kador, L. Optical detection and spectroscopy of single molecules in a solid. *Phys. Rev. Lett.* **62,** 2535–2538 (1989).
7. Basché, T., Moerner, W. E., Orrit, M. & Wild, U. P. *Single Molecule Optical Detection, Imaging and Spectroscopy* (VCH, Weinheim, Germany, 1997).
8. Kopelman, R. & Tan, W. Near-field optics: imaging single moelcules. *Science* **262,** 1382–1384 (1993).
9. Sekatskii, S. K. & Letokhov, V. S. Single fluorescence centers on the tips of crystal needles: first observation and prospects for application in scanning one-atom fluorescence microscopy. *Appl. Phys. B* **63,** 525–530 (1996).
10. Orrit, M. & Bernard, J. Single pentacene molecules detected by fluorescence excitation in a *p*-therphenyl crystal. *Phys. Rev. Let.* **65,** 2716–2719 (1990).
11. Betzig, E., Finn, P. L. & Weiner, J. S. Combined shear force and near-field scanning optical microscope. *Appl. Phys. Lett.* **60,** 2484–2486 (1992).
12. Gross Levi, B. Progress made in near-field imaging with light from a sharp tip. *Phys. Today* **52,** 18–20 (1999).
13. Michaelis, J. *et al.* A single molecule as a probe of the optical intensity distribution. *Opt. Lett.* **24,** 581–583 (1999).
14. Bingelli, M. *et al.* Novel design for a compact fiber optic scanning force microscope. *Rev. Sci. Instrum.* **64,** 2888–2891 (1993).
15. Karrai, K. & Grober, R. D. Piezoelectric tip-sample distance control for near-field optical microscopes. *Appl. Phys. Lett.* **66,** 1842–1844 (1995).
16. Fleury, L., Sick, B., Zumhofen, G., Hecht, B. & Wild, U. P. High photo-stability of single molecules in an organic crystal at room temperature observed by scanning confocal microscopy. *Mol. Phys.* **95,** 1333–1338 (1998).
17. Kulzer, F., Koberling, F., Christ, T., Mews, A. & Basché, T. Terrylene in *p*-terphenyl: single molecule experiments at room temperature. *Chem. Phys.* **247,** 23–34 (1999).
18. Kummer, S., Basché, T. & Bräuchle, C. Terrylene in p-terphenyl: a novel single crystalline system for single molecule spectroscopy at low temperatures. *Chem. Phys. Lett.* **229,** 309–316 (1994).
19. Fischer, U. & Zingsheim, H. P. Submicroscopic pattern replication with visible light. *J. Vac. Sci. Technol.* **19,** 881–885 (1981).
20. Ambrose, P., Basché, T. & Moerner, W. E. Detection and spectroscopy of single pentacene molecules in a *p*-terphenyl crystal by means of fluorescence excitation. *J. Chem. Phys.* **95,** 7150–7163 (1991).
21. Betzig, E., Trautman, J. K., Weiner, J. S., Harris, T. D. & Wolfe, R. Polarization contrast in near-field scanning optical microscopy. *Appl. Opt.* **31,** 4563–4568 (1992).
22. Huser, T., Novotny, L., Lacoste, T., Eckert, R. & Heinzelmann, H. Observation and analysis of near-field optical diffraction. *J. Opt. Soc. Am. A* **16,** 141–148 (1999).
23. Martin, O. J. F., Girard, C. & Dereux, A. Generalized field propagator for electromagnetic scattering and light confinement. *Phys. Rev. Lett.* **74,** 526–529 (1995).
24. Martin, O. J. F. 3D simulations of the experimental signal measured in near-field optical microscopy. *J. Microscopy* **194,** 235–239 (1999).
25. Novotny, L. Single molecule fluorescence in inhomogeneous environments. *Appl. Phys. Lett.* **69,** 3806–3808 (1996).
26. Henkel, C. & Sandoghdar, V. Single molecule spectroscopy near structured dielectrics. *Opt. Comm.* **158,** 250–258 (1998).
27. Harootunian, A., Betzig, E., Issacson, M. & Lewis, A. Super-resolution fluorescence near-field scanning optical microscopy. *Appl. Phys. Lett.* **49,** 674–676 (1986).
28. Barchiesi, D., Pagnot, T., Pieralli, C. & Van Labeke, D. Fluorescence scanning near-field microscopy (FSNOM) by measuring the decay-time of a fluorescent particle. *Proc. SPIE* **2384,** 90–100 (1995).
29. Kulzer, F., Kummer, S., Matzke, R., Bräuchle, C. & Basché, T. Single molecule optical switching in terrylene in *p*-terphenyl. *Nature* **387,** 688–691 (1997).

Acknowledgements

We are grateful to O. Martin and C. Henkel for many fruitful discussions. We thank B. Eiermann for contribution to the initial phase of the experiment, T. Kalkbrenner for the fabrication of the sample, and H. M. Ludwig for the AFM image in Fig. 2. We also thank P. Leiderer and his co-workers, and colleagues at Omicron Vakuum GmbH for help and

advice regarding the construction of the piezo-driven translation stages. J. M. acknowledges a fellowship from the Carl-Zeiss-Schott Förderstiftung. This work was supported by the Deutsche Forschungsgemeinschaft and the Bundesministerium für Bildung und Forschung.

Correspondence and requests for materials should be addressed to V.S. (e-mail: vahid.sandoghdar@uni-konstanz.de).

Intercalation of alkylamines into an organic polymer crystal

Akikazu Matsumoto*, Toru Odani*, Kazuki Sada†, Mikiji Miyata† & Kohji Tashiro‡

* *Department of Applied Chemistry, Faculty of Engineering, Osaka City University, Sugimoto, Sumiyoshi-ku, Osaka 558-8585, Japan*
† *Graduate School of Engineering, Osaka University, 2-1 Yamadaoka, Suita, Osaka 565-0871, Japan*
‡ *Department of Macromolecular Science, Graduate School of Science, Osaka University, Toyonaka, Osaka 560-0043, Japan*

Organic solid-state synthesis allows formation of products that are difficult or impossible to produce by conventional methods. This feature, and the high degree of reaction selectivity that can be achieved, is a direct result of the control over the relative orientation of the reactants afforded by the solid state. But as the successful development of 'topochemical reactions' requires the careful design of suitable reactant crystals, the range of both reactions and products amenable to this approach has been limited[1,2]. However, recent advances in organic crystal engineering, particularly the rational design of complex solid architectures through supramolecular preorganization[3–9], have renewed interest in topochemical reactions. Previously, we have orientated muconate monomers—diene moieties with a carboxylate group on each end—using long-chain *n*-alkylammonium ions, such that the topochemical photopolymerization of the solid-state reactants produces layered crystals of stereoregular and high-molecular-mass polymers[10–13]. Here we show that these polymer crystals are capable of repeated, reversible intercalation[14] by conversion to the analogous poly(carboxylic acid), followed by transformation into a number of poly(alkylammonium muconate)s upon addition of the appropriate amine. Introduction of functional groups into these crystals may allow the design of organic solids for applications such as molecular recognition, separation and catalysis, thereby extending the range and practical utility of current intercalation compounds[15–20].

Alkylammonium (*Z,Z*)-muconates undergo polymerization in the crystalline state under photoirradiation. When a higher *n*-alkyl group (carbon number $m \geq 10$) is introduced in the *N*-substituent, the photoproduct is an insoluble polymer crystal (Fig. 1; see Supplementary Information for preparation and polymerization procedures). Derivatives with a lower *n*-alkyl substituent ($m < 10$) favour topotactic isomerization to the corresponding (*E,E*)-isomers. In Table 1, the results of the photopolymerization are given together with the values of 2θ and interplanar distance (d) determined by small-angle powder X-ray diffraction for both monomer and polymer crystals. No peak was observed in the small-angle region for the monomer crystals with $m < 10$, in contrast to the intense peaks at 2–3° for the monomer and polymer crystals with $m \geq 10$ (Fig. 2a). They correspond to 30–45 Å of the d value, which increased in proportion to the number of carbons in the *N*-alkyl group. The topochemically polymerizable (*Z,Z*)-muconates have similar crystal lattice parameters to each other[11,12]: monoclinic, $P2_1/c$, $a = 10.2320$ Å, $b = 4.9310$ Å, $c = 11.4970$ Å, $\beta = 107.146°$, $V = 554.29$ Å^3, $Z = 2$ for the ethyl ester; monoclinic, $P2_1/a$, $a = 10.98$ Å, $b = 4.862$ Å, $c = 17.72$ Å, $\beta = 97.93°$, $V = 936$ Å^3, $Z = 4$ for the benzylammonium salt; and monoclinic, $P2_1/a$, $a = 11.033$ Å, $b = 4.9360$ Å, $c = 18.011$ Å, $\beta = 95.055$, $V = 977.0$ Å^3, $Z = 4$ for the 2-chlorobenzylammonium salt. A lamellar structure of alkylammonium cation and muconate dianion layers is observed in the monomer crystals of the benzylammonium derivatives, and this ordered structure remains during the topochemical polymerization. Polymerization behaviour that depends on the length of the alkyl

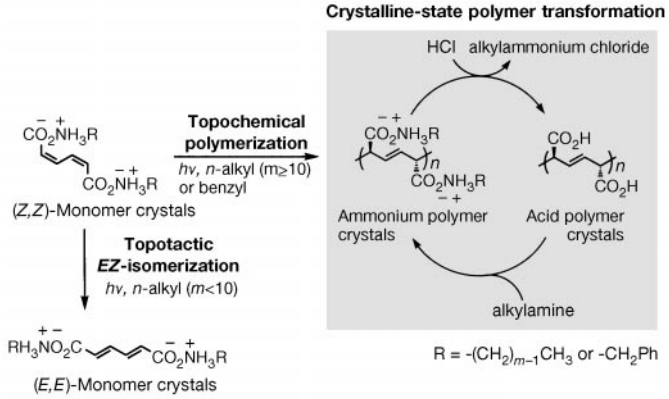

Figure 1 Photoreactions and polymer transformation performed in the crystalline state. Depending on the carbon number of the *n*-alkylammonium group, alkylammonium (*Z,Z*)-muconate undergoes either topochemical polymerization or topotactic *EZ*-isomerization when exposed to photoirradiation in the crystalline state. The ammonium polymer crystals obtained by the topochemical polymerization are converted in the crystalline state to acid polymer crystals via polymer transformation. The reverse reaction from polyacid to the ammonium polymers also occurs.

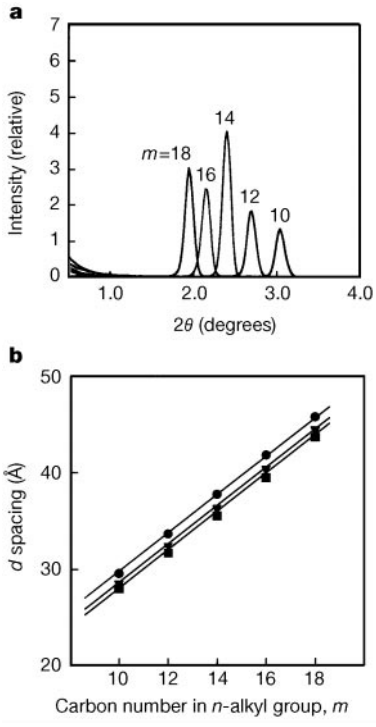

Figure 2 Small-angle X-ray scattering. **a**, Diffraction profiles of poly(*n*-alkylammonium (*Z,Z*)-muconate) crystals as polymerized. **b**, Relationship between the carbon number (m) of the *n*-alkyl group and the d values for *n*-alkylammonium (*Z,Z*)-muconates. Circles, monomer crystals; squares, polymer crystals obtained as polymerized under photoirradiation in the crystalline state after removing unreacted monomers; triangles, polymer crystals obtained by the crystalline-state polymer transformation from poly(muconic acid) with corresponding *n*-alkylamines.